57 years (1960–2017) of snow and meteorological observations from a mid-altitude mountain site (Col de Porte, France, 1325 m of altitude)

Yves Lejeune, Marie Dumont, Jean-Michel Panel, Matthieu Lafaysse, Philippe Lapalus, Erwan Le Gac, Bernard Lesaffre, Samuel Morin

Earth Syst. Sci. Data, 11, 71–88, 2019
https://doi.org/10.5194/essd-11-71-2019

Open Access Earth System Science Data

57 years (1960–2017) of snow and meteorological observations from a mid-altitude mountain site (Col de Porte, France, 1325 m of altitude)

Yves Lejeune, Marie Dumont, Jean-Michel Panel, Matthieu Lafaysse, Philippe Lapalus, Erwan Le Gac, Bernard Lesaffre, and Samuel Morin

Univ. Grenoble Alpes, Université de Toulouse, Météo-France, Grenoble, France, CNRS, CNRM, Centre d'Etudes de la Neige, Grenoble, France

Correspondence: Marie Dumont (marie.dumont@meteo.fr, col_de_porte@meteo.fr)

Received: 20 July 2018 – Discussion started: 15 August 2018
Revised: 7 November 2018 – Accepted: 21 November 2018 – Published: 11 January 2019

Abstract. In this paper, we introduce and provide access to daily (1960–2017) and hourly (1993–2017) datasets of snow and meteorological data measured at the Col de Porte site, 1325 m a.s.l., Chartreuse, France. Site metadata and ancillary measurements such as soil properties and masks of the incident solar radiation are also provided. Weekly snow profiles are made available from September 1993 to March 2018. A detailed study of the uncertainties originating from both measurement errors and spatial variability within the measurement site is provided for several variables. We show that the estimates of the ratio of diffuse-to-total shortwave broadband irradiance is affected by an uncertainty of ± 0.21 (no unit). The estimated root mean square deviation, which mainly represents spatial variability, is ± 10 cm for snow depth, $\pm 25\,\mathrm{kg\,m^{-2}}$ for the water equivalent of snow cover (SWE), and ± 1 K for soil temperature (± 0.4 K during the snow season). The daily dataset can be used to quantify the effect of climate change at this site, with a decrease of the mean snow depth (1 December to 30 April) of 39 cm from the 1960–1990 period to the 1990–2017 period (40 % of the mean snow depth for 1960–1990) and an increase in temperature of $+0.90$ K for the same periods. Finally, we show that the daily and hourly datasets are useful and appropriate for driving and evaluating a snowpack model over such a long period. The data are placed on the repository of the Observatoire des Sciences de l'Univers de Grenoble (OSUG) data centre: https://doi.org/10.17178/CRYOBSCLIM.CDP.2018.

1 Introduction

The Col de Porte (CDP) site is a mid-elevation meadow site located at 1325 m altitude (45.30° N, 5.77° E) in the Chartreuse mountain range. This observation site has been operated since 1959 in collaboration with several academic and non-academic partners (https://www.umr-cnrm.fr/spip.php?rubrique218; last access: 3 December 2018). Daily measurements of snow depth, air temperature, and precipitation amount have been performed since 1960. Hourly measurements of meteorological and snow variables required to run and evaluate detailed snowpack model such as Crocus (Brun et al., 1992; Vionnet et al., 2012) started in 1987 and have been almost continuous during the snow season since the snow season of 1993–1994. Measured data are manually and automatically checked and corrected using the measurements of several sensors and meteorological analyses (SAFRAN, Durand et al., 1999) if required, thus ensuring the quality and continuity of the dataset.

Such a dataset provides a unique framework to drive and evaluate snowpack models over a long period. Indeed Essery et al. (2013) demonstrated that the evaluation of snowpack models can be misleading if performed over only a few snow seasons. In recent years, such datasets with varying levels of detail have been made public for several snow sites (e.g. Essery et al., 2016) and have motivated the publication of a special issue in *Earth System Science Data* to gather openly available detailed meteorological and hy-

drological observational archives from long-term research catchments in well-instrumented mountain regions around the world, such as the Col du Lac Blanc dataset (Guyomarc'h et al., 2019). This initiative arises from a GEWEX Hydroclimatology Panel cross-cut project, INARCH (available at: http://www.usask.ca/inarch, last access: 3 December 2018), the International Network for Alpine Research Catchment Hydrology.

CDP is part of several observation networks at the local level (Observatoire des Sciences de l'Univers de Grenoble, OSUG) and at the national scale (Observation pour l'Experimentation et la Recherche en Environnement CryObsClim and Systèmes d'Observation et d'Expérimentation au long terme pour la Recherche en Environnement des glaciers, GlacioClim) and contributes to OZCAR (Observatoires de la Zone Critique: Applications et Recherches), one of the French components of the ILTER European Research Infrastructure (International Long-term Ecological Research Networks, Gaillardet et al., 2018). It is also a reference station of the World Meteorological Organization (WMO) Global Cryosphere Watch CryoNet network and of the INARCH network. CDP snow and meteorological observations have been selected as an indicator of climate change effects at medium elevation by the National Climate Change Observatory (ONERC, available at: https://www.ecologique-solidaire.gouv.fr/impacts-du-changement-climatique-montagne-et-glaciers, last access: 3 December 2018). The CDP dataset has been used as driving and evaluation data in several snow model intercomparison projects: SnowMIP (Etchevers et al., 2004) and ESM-SnowMIP (Krinner et al., 2018). CDP is also an ideal place for specific snow-related measurement campaigns, e.g. the WMO Solid Precipitation Intercomparison Experiment (SPICE, available at: http://www.wmo.int/pages/prog/www/IMOP/intercomparisons/SPICE/SPICE.html, last access: 3 December 2018), measurement of the spectral reflectance of snow (Dumont et al., 2017; Tuzet et al., 2017), snow surface roughness (Picard et al., 2016), and snow in forested areas (Sicart et al., 2017).

The objectives of the present paper are (i) to extend the hourly dataset published in Morin et al. (2012) from 1993–2011 to 1993–2017, (ii) to provide a daily dataset over the 1960–2017 period, and (iii) to provide estimates of the uncertainties of several variables due to both spatial variability within the observation site and measurement uncertainties. The paper first describes the site and the dataset. The second section is dedicated to providing estimates of measurement uncertainties and spatial variability within the site, and the last section describes some examples of the use of this dataset.

Figure 1. Picture of the site taken on 10 March 2014 from the south barrier, looking towards north.

2 Data description

The Col de Porte site (Fig. 1) is a grassy meadow surrounded by mainly coniferous (spruces) and some lobed-leaf trees. All the instruments are located within an area of $40 \times 50\,m^2$ (Fig. 2, Tables 2, 3, 4). The height of the trees ranges from 10 to 40 m. Note that all datasets are provided in Universal Time Coordinated (UTC).

2.1 Radiation masks

Surrounding trees and topography mask part of the shortwave radiation. Masks were measured at location 31 (Fig. 2) (corresponding to the measurements of the incoming shortwave radiation, see Fig. 2 and Table 2) with 5° resolution in azimuth for two dates: July 1998 (using a theodolite) and June 2018 (using a compass and a clinometer). Masks are provided as a csv file (https://doi.org/10.17178/CRYOBSCLIM.CDP.2018. SolarMask); they contain three values for each azimuth that correspond to lower elevation, upper elevation, and occultation percentage (p_{occ}, visually estimated), defined as follows (Fig. 3). Below the lower mask elevation, there is no direct radiation. Above the upper mask elevation, 100 % of the direct radiation is available, and between the two, only $100 - p_{occ}$ % of the direct radiation is available. These masks are applied for the calculation of the direct and diffuse shortwave incoming radiation as explained in Sect. 2.3.1. The discrepancies between the two masks are most likely due to changes of the vegetation (growing and major tree cutting in 1999, see Morin et al., 2012).

2.2 Soil and vegetation properties

Soil properties were measured close to location 33 (Fig. 2) on 29 September 2008, close to location 24 (Fig. 2) on 2 October 2012, and close to location 30 on 18 October 2017.

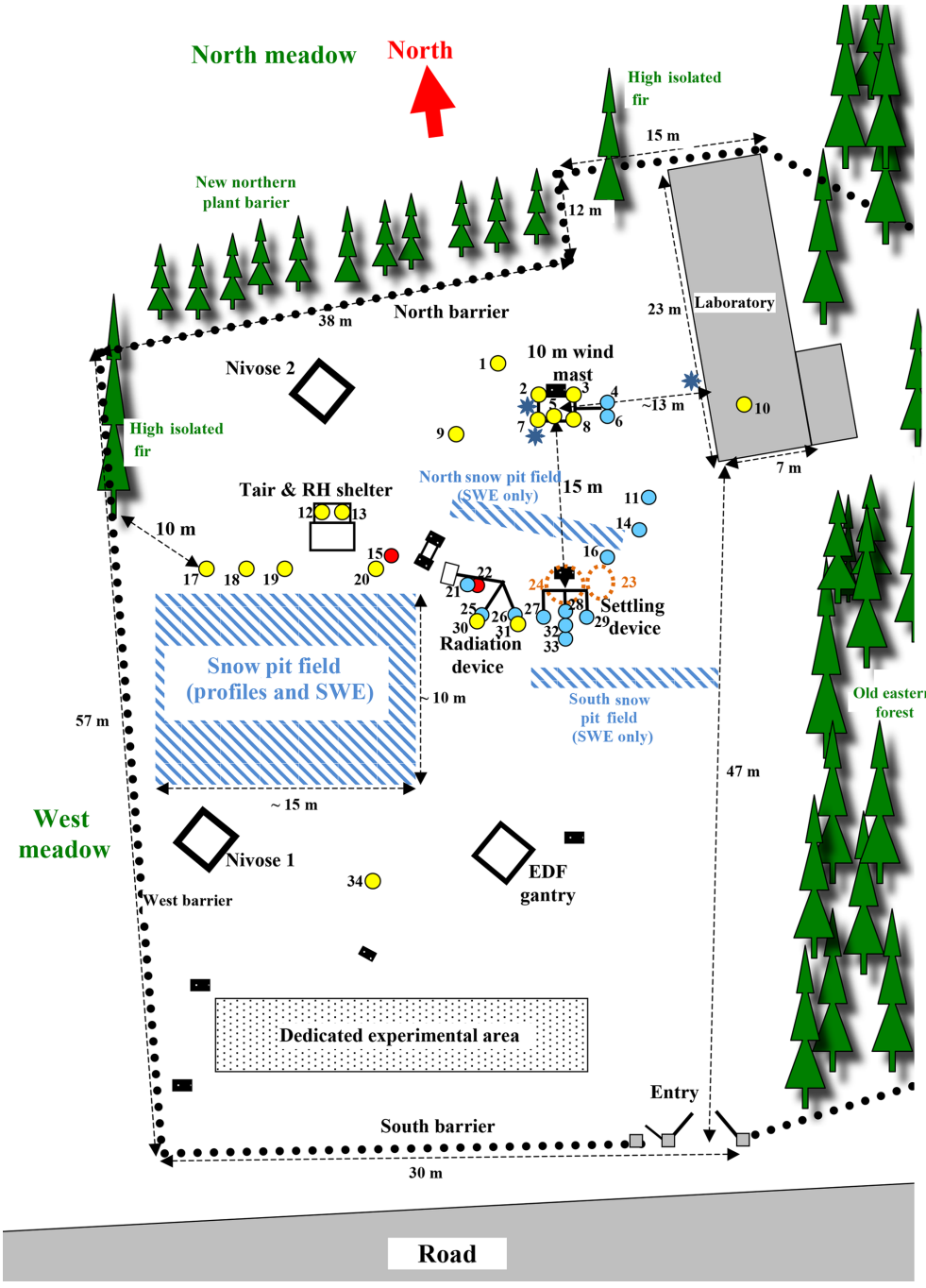

Figure 2. Schematic view of the experimental sites with sensor locations. The sensors indicated in yellow are for meteorological variables. The sensors indicated in red are not used anymore as of 2018, and those in blue correspond to snow measurements. Areas 23 and 24 correspond to soil temperature and humidity measurements. The correspondence between numbering and sensors is indicated in Tables 2, 3, and 4. The three dark blue asterisks correspond to the three hemispherical webcam locations. The dedicated experimental area has been used for specific experiments, e.g. Dumont et al. (2017) and Bouilloud and Martin (2006).

On 29 September 2008, the soil properties were measured over the first metre as illustrated by Fig. 4. The layering of the soil was estimated visually and is provided in Table 1. The soil properties (particle size analysis, organic matter, nitrogen, and carbon total content) were also analysed down to 87 cm depth. The dataset is provided as a csv file (soil_properties_2008.csv). On 2 October 2012, the same analysis was conducted over the first 30 cm of soil at location 24 (Fig. 2) along with measurements of the dry soil density. The dataset is provided as a csv file

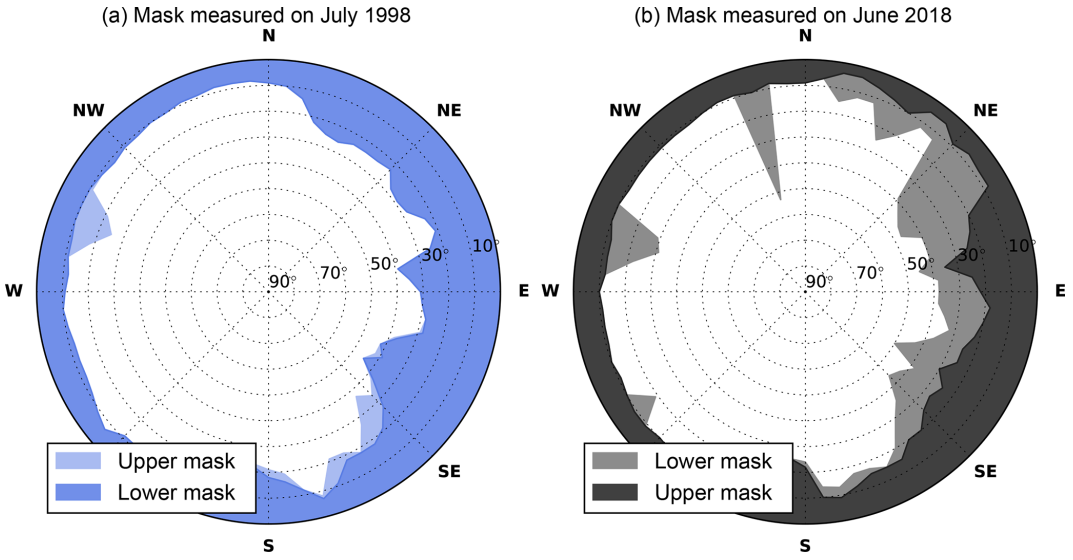

Figure 3. Masks measured at location 31 (Fig. 2) on July 1998 **(a)** and on June 2018 **(b)**. Upper and lower mask elevations are represented by the coloured areas. Elevations are given in degrees, the centre is 60° elevation.

Table 1. Visual characterization of the soil layers corresponding to Fig. 4 on 29 September 2008.

Top depth (cm)	Bottom depth (cm)	Visual texture
0	5	organic soil with grass roots
5	18	organic soil without roots
18	47	clay and sand
47	70	grey clay and sand
70	87	grey clay
87	100	pebbles and grey clay, no sampling

(soil_properties_2012.csv). The two csv files are available as https://doi.org/10.17178/CRYOBSCLIM.CDP.2018.Soil.

On 18 October 2017, the soil densities were analysed for the first 30 cm. At that time, the dry soil density was $1100 \pm 67\,\mathrm{kg\,m^{-3}}$ without considering the vegetation. The wet soil density was $1475 \pm 59\,\mathrm{kg\,m^{-3}}$. These values are the mean and standard deviation of two measurements over 0–10 cm depth and two measurements at 20–30 cm depth close to location 30 (Fig. 2). No significant differences between the two sampling depths were observed. On the same day, the vegetation's (grass) dry and wet mass were measured on a 50 by 50 cm surface at the same location. The measurements result in a value of $1.92\,\mathrm{kg\,m^{-2}}$ for wet mass and $1.54\,\mathrm{kg\,m^{-2}}$ for dry mass. The height of the grass (roughly 5 cm) during the time of the measurements can be considered typical for late autumn. Note that the grass is frequently cut during summer. These measured soil and vegetation properties can be useful for constraining soil and vegetation schemes, which are often coupled with snowpack models (Decharme et al., 2013).

Figure 4. Soil profile of 1 m depth performed close to location 33 (Fig. 2) on 29 September 2008. The visual characterization provided in Table 1 can be seen on this picture.

2.3 Meteorological hourly data, 1993-2017

The meteorological hourly dataset over 1993–2017 is an extension of the meteorological dataset provided in Morin et al. (2012), in which an extensive description of the dataset is available. Below, only changes that happened after 2011 and additional details not provided in Morin et al. (2012) are reported.

The dataset is provided as a continuous hourly dataset since 1993 so that it can be easily used to drive snowpack models. The partitioning of the dataset between in situ data and the output of the meteorological analysis and downscaling tool SAFRAN (Durand et al., 1999, 2009b) is the same as in Fig. 4 of Morin et al. (2012). For years 2011 to 2015, in situ data are restricted to the period of 20 October of one year to 10 June of the next year. Summer in situ data are thus missing (calibration of the sensors during summer) from 1993 to 2015. Starting on 10 June 2015, all data are in situ year-round except for very short periods with observation issues. An in situ flag is provided together with the meteorological data (value = 1 for in situ data).

Table 2 provides an update of the type of sensors used for meteorological measurements with respect to Table 1 in Morin et al. (2012). The dataset is provided in netCDF format (https://doi.org/10.17178/CRYOBSCLIM.CDP.2018.MetInsitu) in the standard format for SURFEX surface model meteorological inputs (Vionnet et al., 2012; Masson et al., 2013). The atmospheric pressure value corresponds to the mean climatological value at CDP.

2.3.1 Shortwave incoming radiation

The meteorological dataset provides both total and diffuse incoming broadband radiation at location 31 (Fig. 2). The diffuse shortwave radiation is not measured but calculated from total shortwave and longwave incident radiation and air temperature as described in the following.

The first step of the procedure is to compute a cloudiness value, η (no unit, between 0 for clear sky and 1 for fully overcast), from measured air temperature T_{air} (K), longwave radiation $\mathrm{LW}_{\mathrm{down}}$ ($\mathrm{W\,m^{-2}}$), and specific humidity using Eqs. (1) and (2) from Berliand (1952) and Etchevers (2000):

$$\mathrm{LW}_{\mathrm{down}} = 1.05\varepsilon\sigma T_{\mathrm{air}}^4, \quad (1)$$

$$\varepsilon = 0.58 + 0.9k(\eta) + 0.06\sqrt{e_{\mathrm{air}}}(1 - k(\eta)), \quad (2)$$

$$k(\eta) = (0.09 + 0.2\eta)\eta^2, \quad (3)$$

where σ is the Stefan–Boltzmann constant, and e_{air} is the water vapour partial pressure calculated from measured T_{air} and relative humidity, expressed in hectopascals. The correction factor 1.05 in Eq.(1) accounts for the additional longwave radiation that is reaching the sensor due to the presence of surrounding trees. Equation (2) solution does not necessarily range between 0 and 1; η must be bounded between 0 and 1 when solving the equation.

The calculated value of η is then used to partition the total measured shortwave radiation into direct and diffuse fractions using the radiative transfer model from Vauge (1983) and the measured mask described in Sect. 2.

An additional shortwave radiation sensor (Delta-T SPN1 – heated) was installed at location 5 (Fig. 2) in September 2016 (9.5 m above ground) and measures both diffuse and total shortwave radiation over the 400–2700 nm range.

A comparison between these measured and calculated direct and diffuse distributions is provided in Sect. 3.1.

2.3.2 Longwave incident radiation

The sensor for incident longwave radiation was replaced in October 2015 by a Kipp & Zonen CGR4 sensor (location 30, Fig. 2). Figure 5 displays the comparison of the measured incident longwave radiation with simulated longwave radiation from SAFRAN based on monthly averages. It shows that the deviation between SAFRAN and the measurements displays two large breaks in October 2015 and in autumn 2010 (corresponding to another sensor replacement, Table 2). Based on the hypothesis that the newest sensor can be used as a reference because it was fully calibrated at the Physikalisch-Meteorologisches Observatorium (Davos, Switzerland) outside and inside with a blackbody, the dataset was corrected as follows: $-10\,\mathrm{W\,m^{-2}}$ from 1993 to November 2010 and $+10\,\mathrm{W\,m^{-2}}$ from November 2010 to November 2015. Since SAFRAN is the only available reference and does not account for local conditions, e.g. cloudiness, due to its coarse spatial resolution, it is unfortunately not possible currently to investigate this instrumental bias with more temporal refinement. This correction, although spanning the uncertainty values provided by the manufacturer, is of large significance for snowpack modelling, considering the high sensitivity of the snowpack to processes governed by this variable (e.g. Raleigh et al., 2015; Sauter and Obleitner, 2015; Quéno et al., 2017). Using the Crocus snowpack model with or without the corrections leads to a shift in the melt-out date ranging between 5 and 10 days.

2.3.3 Precipitation

Precipitation data are handled according to Morin et al. (2012). Precipitation data are manually partitioned between liquid and solid phases using all relevant sources of data at the site, namely snow depth, surface albedo, surface and air temperatures, and differences between heated and non-heated rain gauges (locations 1 and 9, Fig. 2). The precipitation values provided in the dataset are based on the reference gauge (GEONOR) at location 20 (Fig. 2). Other OTT and GEONOR gauges are used to complement the reference sensor measurements. Hourly solid precipitation measurements are corrected for undercatch depending on temperature and wind speed, as described in Morin et al. (2012). From 2013 to 2017, the wind measurement used for the correction was

Table 2. Overview of the sensors used to gather the hourly meteorological data between 1993 and 2017 at Col de Porte, France. The locations refer to Fig. 2.

Variable	Location	Sensor	Period of operation	Height	Unit	Integration method
Air temperature	12	PT100, 3 wires	...→ 1996–1997	1.5 ma	K	Instantaneous
	12	PT100, 4 wires	1997–1998 → ...	1.5 ma	K	Instantaneous
	mast	PT100, 4 wires	1997–1998 → ...	3.1 m	K	Instantaneous
Relative humidity	13	SPSI MU-C.1/MUTA.2	...→ 1994–1995	1.5 ma	%RH	Instantaneous
	13	Vaisala HMP35DE	1995–1996 → 2005–2006	1.5 ma	%RH	Instantaneous
	13	Vaisala HMP45D	2006–2007 →...	1.5 ma	%RH	Instantaneous
Wind speed	2	Laumonier – heated	1997–1998 →...	10 m	$m\,s^{-1}$	Integrated (60 min)
	7	Chauvin Arnoux Tavid 87 – non-heated	whole record	10 m	$m\,s^{-1}$	Integrated (60 min)
	15	Laumonier – heated	Sept 2000 → June 2015	3.3 m	$m\,s^{-1}$	Integrated (60 min)
	3	Thies ultrasonic anemometer – heated	Mar 2012 →...	10 m	$m\,s^{-1}$	Integrated (60 min)
	18	Thies ultrasonic anemometer – heated	Dec 2013 →...	3.3 m	$m\,s^{-1}$	Integrated (60 min)
Inc. shortwave radiation	31	Kipp & Zonen CM7	...→ 15 Mar 1996	1.2 ma	$W\,m^{-2}$	Integrated (50 min)
	31	Kipp & Zonen CM14	15 Mar 1996 → 31 Oct 2015	1.2 ma	$W\,m^{-2}$	Integrated (50 min)
	31	Kipp & Zonen CMP10	Nov 2015 →...	1.2 ma	$W\,m^{-2}$	Integrated (50 min)
Inc. longwave radiation	30	Eppley PIR	...→ 2010–2011	1.2 ma	$W\,m^{-2}$	Integrated (50 min)
	30	Kipp & Zonen CG4	2010–2011 → Oct 2015	1.2 ma	$W\,m^{-2}$	Integrated (50 min)
	30	Kipp & Zonen CGR4	Oct 2015→...	1.2 ma	$W\,m^{-2}$	Integrated (50 min)
Precipitation	9	PG-2000 – heated (2000 cm^2), tipping bucket	whole record	2.75 m	$kg\,m^{-2}\,s^{-1}$	Difference
	1	PG-2000 – non-heated (2000 cm^2), tipping bucket	whole record	2.75 m	$kg\,m^{-2}\,s^{-1}$	Difference
	20	GEONOR (200 cm^2) with windshield, weighing gauge	whole record	3 m	$kg\,m^{-2}\,s^{-1}$	Difference
	17b	GEONOR T-200B-3 (200 cm^2), weighing gauge	Dec 2013 →...	3.1 m	$kg\,m^{-2}\,s^{-1}$	Difference
	19b	GEONOR T-200B-3 (200 cm^2) with windshield, weighing gauge	Dec 2013 →...	3.1 m	$kg\,m^{-2}\,s^{-1}$	Difference
	34b	OTT Pluvio 2 (400 cm^2) with windshield, weighing gauge	Dec 2013 →...	3.1 m	$kg\,m^{-2}\,s^{-1}$	Differencec

* Height adjusted manually above snow surface (≈ weekly). ◇ The sensors were installed for the WMO SPICE project and are used in this study only to complement the dataset if a problem exists for the reference sensor. c Amount processed in non-real-time (filtered values).

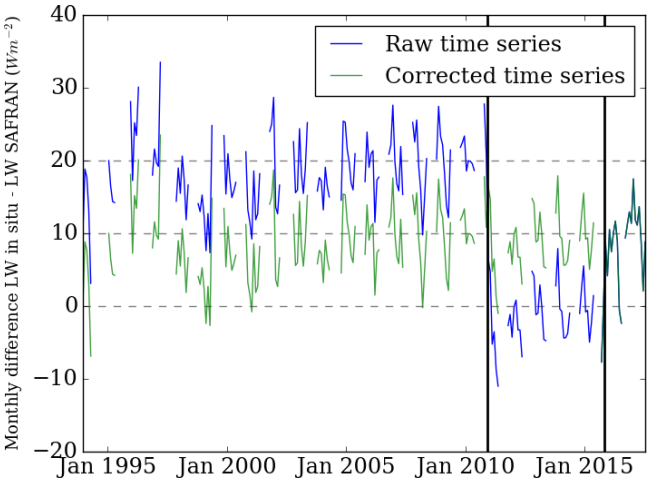

Figure 5. Monthly average of the difference between measured downward longwave (LW) and SAFRAN estimates. The two vertical black lines indicate the sensor changes (cf. Table 2). The blue lines correspond to the raw time series and the green one to the corrected time series.

the one placed at location 18 (Fig. 2) instead of location 15 (Fig. 2) since the ultrasonic sensor at location 18 (Fig. 2) is more accurate than the wind sensor at location 15 (Fig. 2). Note that locations 15 and 18 are very close, i.e. a few metres, so that the wind speed values are not significantly different between the two locations.

2.4 Snow and soil data, 1993–2017

The hourly evaluation dataset over 1993–2017 is an extension of the evaluation dataset provided in Morin et al. (2012). An extensive description of the dataset is available in the latter study. Below, only changes that happened after 2011 and additional details not provided in Morin et al. (2012) are reported. The hourly dataset is provided as a netCDF file (https://doi.org/10.17178/CRYOBSCLIM.CDP.2018.HourlySnow). Within this dataset, the soil temperature, soil humidity, and settling disk temperature are raw measurements (uncorrected).

Table 3 provides an update of the type of sensors used for evaluation measurements with respect to Table 2 in Morin et al. (2012).

Starting in October 2010, the snow depth at location 32 (Fig. 2) has been measured with a Dimetix laser ranger. The field of view is a few millimetres in diameter and the accuracy provided by the manufacturer is ±1.5 mm. Since October 2010, the snow depth measurement provided in the dataset (reference snow depth) is the measurement of the Dimetix laser ranger. Data from the other snow depth sensors and precipitation amounts are used to correct the laser data from small artefacts.

The surface temperature reference values contained in the dataset mainly originate from the Kipp & Zonen upward pyrgeometer (location 25, Fig. 2, same sensor as location 30, Fig. 2 and Table 2). Since September 2010, these data have been complemented by the other surface temperature sensors with a conical field of view shown in Table 3. The reference surface temperature is bounded to 273.15 K when snow is present on the ground.

New sensors for soil temperature and humidity have been installed in October 2012 at several depths (−0.05, −0.1, −0.2, −0.3 m) at location 23 (Fig. 2) close (roughly 2 m) to location 24 (Fig. 2), where the older soil temperature sensors were located. In total, for location 23 (Fig. 2), three probes are placed at 10 cm depth, roughly 10 cm away from each other. In the following, they are referred as s1_loc23_10, s2_loc23_10, and s3_loc23_10. At 20 cm depth, there are only two probes roughly 10 cm away from each other that are referred as s1_loc23_20 and s2_loc23_20.

The differences between the measurements at these two locations are discussed in Sect. 3.4. It must be underlined that the soil humidity measurements show that the soil is almost always saturated by liquid water when snow is present. This characteristic may not be typical for mountain slopes (e.g. Williams et al., 2009) and may be difficult to reproduce with usual soil models.

The measurements of the vertical profile of snowpack properties as described in Fierz et al. (2009) are also provided in caaml format (version 6) according to the International Association of Cryospheric Sciences (IACS) standard (http://caaml.org/Schemas/SnowProfileIACS/v6.0.3/index.html, last access: 3 December 2018). They can be visualized using Niviz software (https://niviz.org/, last access: 3 December 2018). An example is displayed in Fig. 6 for 13 January 2001. These profiles are available on a weekly basis from September 1993 to March 2018 (https://doi.org/10.17178/CRYOBSCLIM.CDP.2018.SnowProfile).

2.5 1960–2017 data

Table 4 describes the daily dataset that combines snow and meteorological measurements. The dataset is provided in netCDF format (https://doi.org/10.17178/CRYOBSCLIM.CDP.2018.MetSnowDaily). Variable names correspond to the names listed in Table 4. Within this daily dataset, the total precipitation dataset is not corrected for undercatch, contrary to rain and snow datasets (starting in September 1993). The total precipitation dataset is also not measured by the same sensor used for the rain and snow datasets (cf. Table 4). The total precipitation dataset is measured with a PG-2000 sensor, for which the undercatch plays a minor role compared to the GEONOR due to the collecting surface area being 10 times larger (Table 2). In addition, the total precipitation time series may be qualified as inhomogeneous in time due to the various changes in precipitation gauges. The daily SWE (water equivalent of snow cover) automatic measurements

Table 3. Overview of the sensors used to gather the hourly and daily snow and soil data between 1993 and 2017 at Col de Porte, France. Note that outgoing shortwave and longwave radiation is measured using instruments similar to the corresponding incoming radiation, described in Table 2. Also note that snow surface temperature can be derived from the outgoing longwave radiation sensor in addition to the sensors presented here. The locations refer to Fig. 2.

Variable	Location	Sensor	Period of operation	Height	Unit	Time resolution	Integration method
Snow depth	33	BEN ultrasonic depth gauge	... → 1999–2000	3 m	m	hourly	Instantaneous
	33	FNX ultrasonic depth gauge	2000–2001 → 2008–2009	3 m	m	hourly	Instantaneous
	33	Campbell ultrasonic depth gauge SR50A	2009–2010 → ...	3.5 m	m	hourly	Instantaneous
	32	Dimetix laser ranger	2010–2011 → ...	3.1 m	m	hourly	Instantaneous
	6d	Campbell ultrasonic depth gauge SR50	Jan 2014 → ...	4.1 m	m	hourly	Instantaneous
	6d	Campbell ultrasonic depth gauge SR50ATH	Jan 2014 → ...	4.1 m	m	hourly	Instantaneous
	6d	Jenoptik laser ranger	Jan 2014 → ...	4.1 m	m	hourly	Instantaneous
	6d	Dimetix laser ranger	Jan 2014 → ...	4.1 m	m	hourly	Instantaneous
	hatched	Snow pit (up to three values)	whole record	N.A.	m	≈ weekly	N.A.
Water equivalent of snow cover	16	cosmic ray neutron sensor	2001–2002 → ...	0 m	$kg\,m^{-2}$	daily	24 h integration
	16	cosmic ray neutron sensor[a]	2008–2009 → ...	0 m	$kg\,m^{-2}$	daily	24 h integration
	hatched	Snow pit (up to three values)	whole record	N.A.	$kg\,m^{-2}$	≈ weekly	N.A.
Run-off	11	5 m^2 lysimeter, tipping gauge	... → Mar 1994	0 m	$kg\,m^{-2}\,s^{-1}$	hourly	Difference
	11	5 m^2 lysimeter, scale	Mar 1994 → ...	0 m	$kg\,m^{-2}\,s^{-1}$	hourly	Difference
	14	1 m^2 lysimeter, tipping gauge	... → Dec 1996	0 m	$kg\,m^{-2}\,s^{-1}$	hourly	Difference
	14	1 m^2 lysimeter, scale	Dec 1996 → ...	0 m	$kg\,m^{-2}\,s^{-1}$	hourly	Difference
Surface temperature	22	Testo term Pyroterm	... → Oct 2016	1.2 m[b]	K	hourly	Instantaneous
	21	Campbell IR120	Nov 2015 → ...	0.8 m[b]	K	hourly	Instantaneous
	28	Heitronics KT15	2010–2011 → ...	3.2 m	K	hourly	Instantaneous
	4d	Campbell IR120	Jan 2014 → ...	4.1 m	K	hourly	Instantaneous
Soil temperature	24	PT100, 3 wires	...→ 1996–1997	−0.1 m	K	hourly	Instantaneous
	24	PT100, 4 wires	1997–1998 → ...				
	24	PT100, 3 wires	... → 1996–1997	−0.2 m	K	hourly	Instantaneous
	24	PT100, 4 wires	1997–1998 → ...				
	24	PT100, 3 wires	...→ 1996–1997	−0.5 m	K	hourly	Instantaneous
	24	PT100, 4 wires	1997–1998 → ...				
	23	PT100, 4 wires	Oct 2012 → ...	−0.05 m	K	hourly	Instantaneous
	23	PT100, 4 wires	Oct 2012 → ...	−0.10 m	K	hourly	Instantaneous
	23	PT100, 4 wires	Oct 2012 → ...	−0.20 m	K	hourly	Instantaneous
	23	PT100, 4 wires	Oct 2012 → ...	−0.30 m	K	hourly	Instantaneous
Soil moisture	23	Delta-T ML2x ThetaProbe moisture sensor	Oct 2012	−0.05 m	$m^3\,m^{-3}$	hourly	Instantaneous
	23	Delta-T ML2x ThetaProbe moisture sensor	Oct 2012 → ...	−0.10 m	$m^3\,m^{-3}$	hourly	Instantaneous
	23	Delta-T ML2x ThetaProbe moisture sensor	Oct 2012 → ...	−0.20 m	$m^3\,m^{-3}$	hourly	Instantaneous
	23	Delta-T ML2x ThetaProbe moisture sensor	Oct 2012 → ...	−0.30 m	$m^3\,m^{-3}$	hourly	Instantaneous
Settling disks temp.	27 and 29	PT100, 3 wires	... → 1996–1997	variable	K	hourly	Instantaneous
	27 and 29	PT100, 4 wires	1997–1998 → ...				
Settling disks height	27 and 29	In-house positioning system	whole record[c]	variable	m	hourly	Instantaneous
Ground flux	24	Hukseflux HFP01	since 2010–2011	0	$W\,m^{-2}$	hourly	Instantaneous

[a] Sensor including shielding for ground-originating neutrons (reduced data scatter). [b] Height adjusted manually above snow surface (≈ weekly). [c] Progressive migration from mercury to solid state electric contact. ◇ The sensors have been installed for the WMO SPICE project and are used in this study only to complement the dataset if a problem exists for the reference sensor.

Table 4. Description of the daily dataset between 1960 and 2017 at Col de Porte, France. The locations refer to Fig. 2.

Variable	Location	Sensor	Period of operation	Unit	Description
T_{min}	12	PT100	... → 1993	K	Min temp. between 00:00 (day D) and 24:00 (day D)
	12	cf. Table 2	1993 → ...	K	Min temp. between 06:00 (day D−1) and 06:00 (day D)
T_{max}	12	PT100	... → 1993	K	Max temp. between 00:00 (day D) and 24:00 (day D)
	12	cf. Table 2	1993 → ...	K	Max temp. between 06:00 (day D) and 06:00 (day D+1)
snow_depth_auto	close to 33	automatic sensor	... → 1977–1978	m	Snow depth 06:00 (day D)
	33	BEN ultrasonic depth gauge	1978–1979 → 1999–2000	m	Snow depth 06:00 (day D)
	33–6	cf. Table 3	1993 → ...	m	Snow depth 06:00 (day D)
snow_depth_pit	hatched	manual	1963–1964 → 7 Feb 1996	m	Irregular frequency
	hatched	manual	8 Feb 1996 → ...	m	Weekly
snow_depth_pit_north	hatched	manual	2001–2002 →...	m	Weekly
snow_depth_pit_south	hatched	manual	2001–2002 →...	m	Weekly
swe_auto	16	cf. Table 3	2001–2002 →...	$kg\,m^{-2}$	Daily (not available for 2015–2016)
swe_pit	hatched	manual	1963–1964 → 7 Feb 1996	$kg\,m^{-2}$	Irregular frequency, SWE core 38.5 and 25. cm^2
	hatched	manual	8 Feb 1996 → ...	$kg\,m^{-2}$	Weekly, SWE core 100 cm^2
swe_pit_north	hatched	manual	2001–2002 → ...	$kg\,m^{-2}$	Weekly, SWE core 100 cm^2
swe_pit_south	hatched	manual	2001–2002 → ...	$kg\,m^{-2}$	Weekly, SWE core 100 cm^2
total_precipitation	9	cf. Table 2	1960–1961 → 2004–2005	$kg\,m^{-2}$	Daily sum of precipitation not corrected for undercatch 06:00 (day D) to 06:00 (day D+1)
raina	20	cf. Table 2	1993–1994 → ...	$kg\,m^{-2}$	Daily sum of corrected liquid precipitation 06:00 (day D) to 06:00 (day D+1)
snowa	20	cf. Table 2	1993–1994 → ...	$kg\,m^{-2}$	Daily sum of corrected solid precipitation 06:00 (day D) to 06:00 (day D+1)
height of new snow	33 and 27	calculated from snow depth measurement and settlement disks	whole record	cm	Daily sum of new snow 06:00 (day D) to 06:00 (day D+1)
albedo_daily	26 and 31	cf. Table 2	2005–2006 → ...	NA	Ratio of the daily sums of reflected and incident shortwave radiation
albedo_daily_flag	26 and 31	NA	2005–2006 → ...	NA	Number of hourly measurements used to calculate daily albedo

a Note that rain and snow variables are provided only when in situ measurements are available (i.e. in situ flag of Table 2 – see also Fig. 4 in Morin et al., 2012).

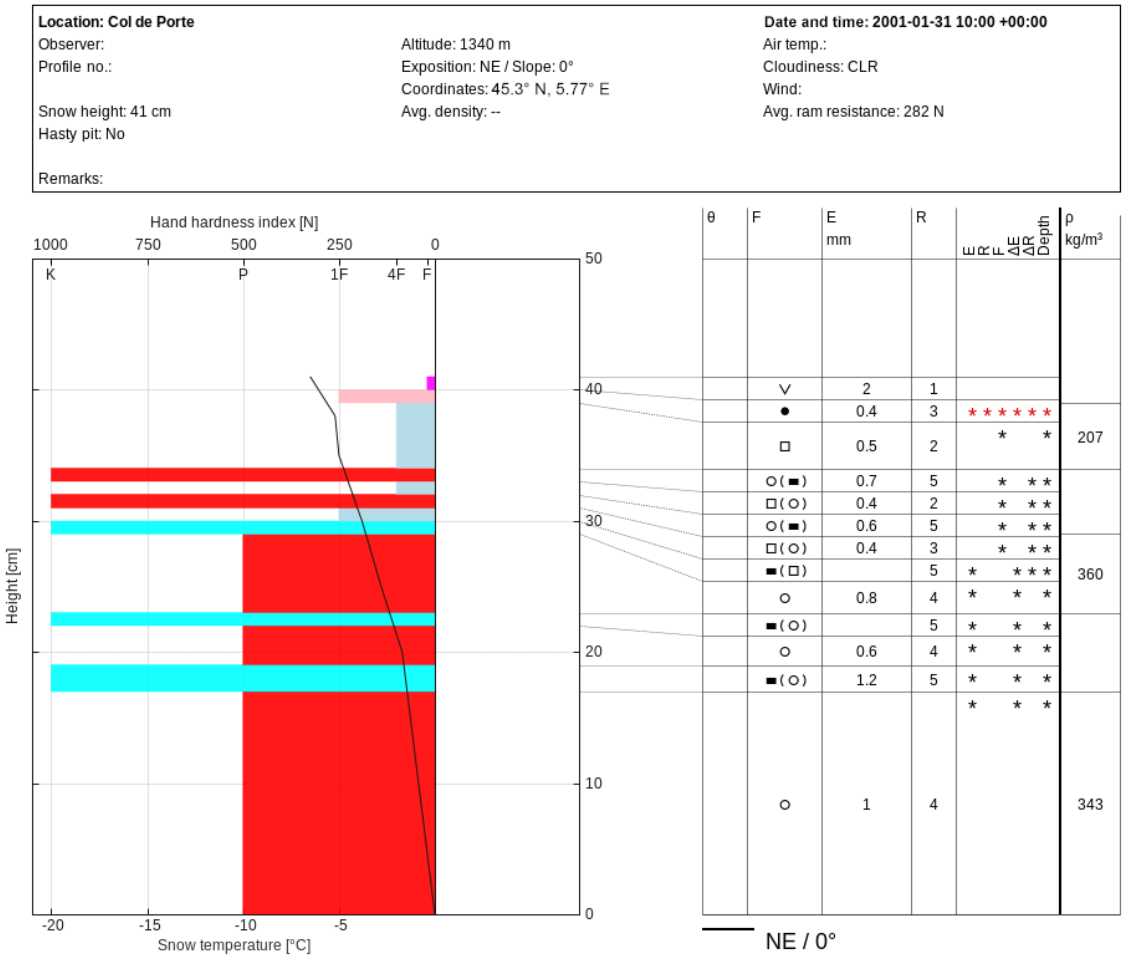

Figure 6. Example of the snow profile measured on 13 January 2001, visualized using Niviz software.

(location 16, Fig. 2, Table 3) are discarded for snow season 2015–2016 due to a disfunction of the sensor. Also note that the daily albedo data are uncorrected for local snow surface slope.

The hourly meteorological dataset that contains the whole SAFRAN reanalysis (Durand et al., 2009a) at Col de Porte for the period of 1960–2017 is provided in order to drive the snowpack simulation over the whole period. The dataset is provided in netCDF format (https://doi.org/10.17178/CRYOBSCLIM.CDP.2018.MetSafran), which is the standard format for SURFEX meteorological inputs (Vionnet et al., 2012; Masson et al., 2013). The solar mask measured in 1998 (Fig. 3) is accounted for in this dataset.

3 Spatial variability and measurement uncertainties

The dataset presented in this study is, like any observation dataset, affected by different sources of uncertainties. Regardless of whether these data are used for model evaluation or process studies, characterizing their associated uncertainties is essential for proper use of the data. The uncertainties of the dataset may come from measurement uncertainties (including instrumental and environmental uncertainties) but also from the spatial variability of the variables within the measurement plot.

A lower bound of the uncertainty for each variable can be estimated from the information provided by the sensor manufacturer. Some variables are measured at different locations within the field sites and by different sensors. This provides a better insight of the uncertainty associated with both sources for each variable. Lafaysse et al. (2017) already provided a first estimate of the uncertainties associated with snow depth, the water equivalent of snow cover, bulk density, broadband albedo, soil temperature, and snow surface temperature. In this section, we extend the period and the number of points used for the uncertainty evaluations for snow depth, the water equivalent of snow cover, and soil temperature, for which several measurements are available over a sufficiently long period. We also provide uncertainty assessments of the di-

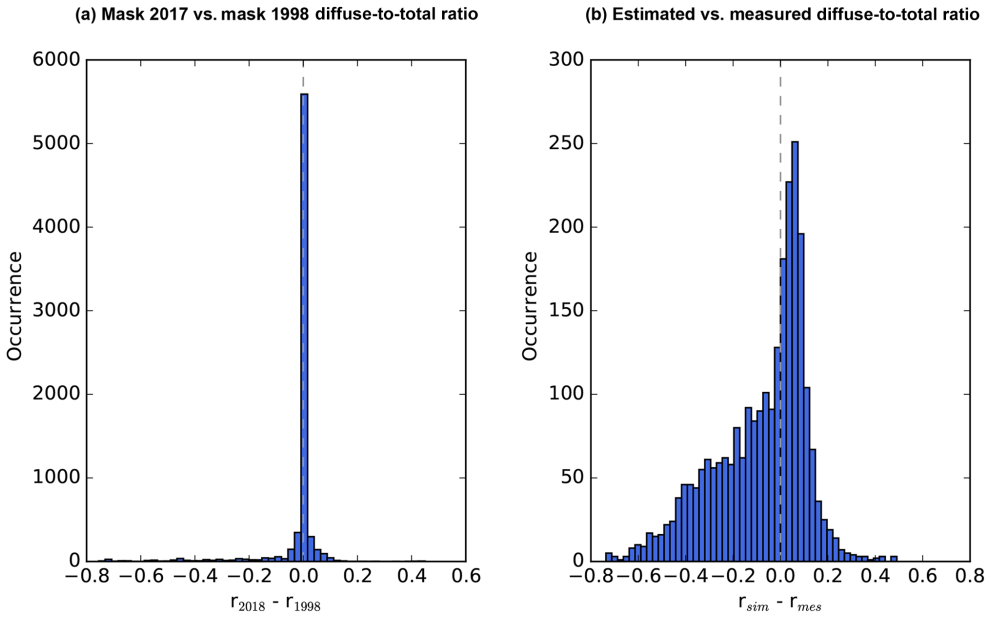

Figure 7. Comparison of different broadband diffuse-to-total shortwave radiation ratios, r. **(a)** Difference in ratio estimated with the mask measured in June 2018 and in June 1998 at location 25 (Fig. 2). Statistics are calculated during daylight from 1 September 2015 to 30 June 2017, excluding July and August for each year. **(b)** Difference in ratio estimated with the 2017 mask (measured at location 5, Fig. 2, 21 October 2017) and the measured ratio at location 5 (Fig. 2). Statistics are calculated during daylight from 1 September 2016 to 30 June 2017.

rect and diffuse incident shortwave radiation estimates (cf. Sect. 2.3.1 for the calculation of the estimates). Note that an update on the uncertainties for snow surface temperature and broadband albedo is not provided in this study (lack of a sufficient number of sensors), though their uncertainty estimates are crucial for snow model evaluation. In this respect, we recommend the use of uncertainty values provided in Lafaysse et al. (2017) for these two variables.

3.1 Direct and diffuse shortwave incoming radiation

A first source of uncertainty in the calculation of the distribution of the measured broadband shortwave radiation into diffuse and direct radiation originates from the uncertainties of the mask used for the calculation (cf. Sect. 2, Fig. 3). Using the methodology explained in Sect. 2.3.1, we estimate the direct and diffuse shortwave incoming radiation based on the mask from 1998 and the mask from 2018 for two snow seasons (1 September to 30 June): 2015–2016 and 2016–2017. The mean difference (mask measured in 2018 minus mask measured in 1998) and root mean square deviation (RMSD) computed between diffuse components (over non-zero values only) are -1.30 and $10.1\,\mathrm{W\,m^{-2}}$. The mean difference and RMSD for the diffuse-to-total ratio are -0.02 and 0.10, respectively. The histogram of differences is provided in Fig. 7a.

The accuracy of the methodology described in Sect. 2.3.1 has also been evaluated using the measurements of total and diffuse radiation from location 5 (Fig. 2) (at 10 m above ground) and the mask measured in October 2017 at the same location. The comparison is done from 1 September 2016 to 30 June 2017 during daylight (i.e. if the total measured shortwave is larger than $4\,\mathrm{W\,m^{-2}}$). The mean difference between the estimated and simulated diffuse component is $-15.26\,\mathrm{W\,m^{-2}}$ (RMSD: $53\,\mathrm{W\,m^{-2}}$). The mean difference and RMSD computed for the diffuse-to-total ratio are -0.08 and 0.21, respectively. The histogram of differences is provided in Fig. 7b. This shows that the estimation of the diffuse radiation has a slightly negative bias and that this uncertainty has to be taken into account for applications such as radiative balance calculation, for which the direct and diffuse distribution has a significant impact. It also shows that the methodology applied to partition the direct and diffuse components has a larger impact on the uncertainty than the change in solar masks shown in Fig. 3.

3.2 Snow depth

Figure 8 compares the snow depth reference value mostly measured at locations 32 and 33 (Fig. 2), h_{ref}, with several other measurements of snow depth: in panel (a) with respect to automatic snow depth measurements at Nivose 1 and location 6 (Fig. 2) and in panel (b) with respect to manual snow depth measurement in snow pit fields (main, north, and south; blue hatched areas in Fig. 2). For panel (a), the comparison is done over the 2009–2016 period, and any blank or incon-

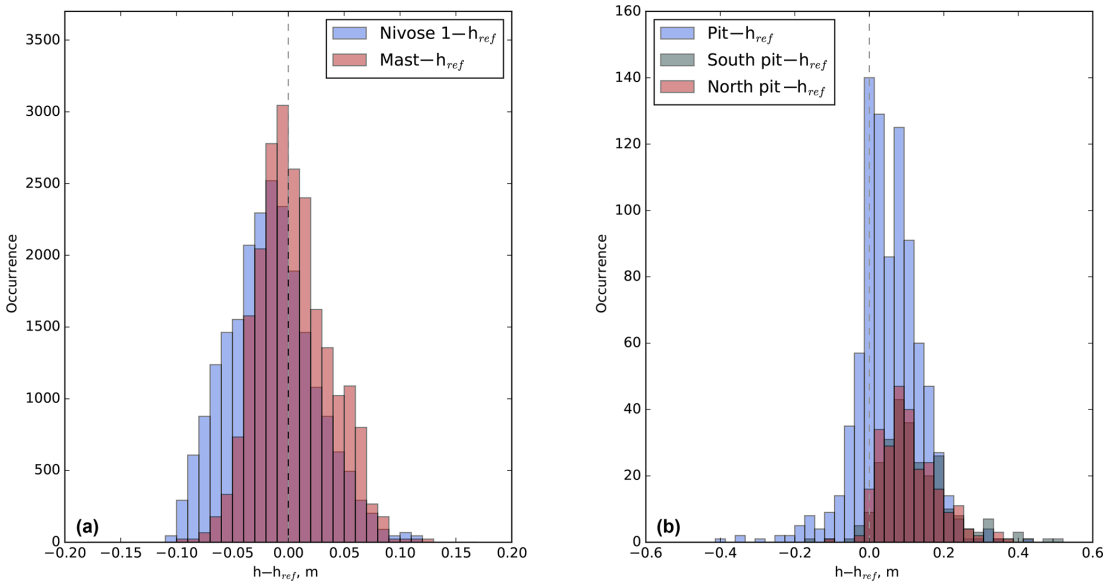

Figure 8. Comparison of snow depth measurements at different locations. The variable h_{ref} corresponds to location 33 (Fig. 2). **(a)** Difference in measured snow depth between the ultrasound sensor placed at the Nivose 1 location (Fig. 2) and the reference snow depth (locations 32–33, Fig. 2) in blue. The differences between the measured snow depth at location 6 (Fig. 2) and the reference snow depth are in red. The differences are calculated from the snow season 2009–2010 to the snow season 2015–2016 using only data from 20 September to 10 June. Data where both locations indicate 0 snow depth are excluded from the statistics. **(b)** Difference in measured snow depth between the manual snow depth measurements at the snow pit field location (Fig. 2) and the automatic reference snow depth (location 33, Fig. 2) in blue, the manual snow depth measurement in the south snow pit field and the reference in grey, and the north snow pit field and the reference in red. Difference values are calculated over the 1960–2017 period for the pit value and over the 2001–2017 period for the north and south pits. Data where both locations indicate 0 snow depth are excluded from the statistics. Corresponding statistics are provided in Table 5.

Table 5. Statistics of the comparisons between the different snow depth measurements represented in Fig. 8.

Sensors	Number of times	Deviation (m)	RMSD (m)	Period
Nivose 1–h_{ref}	22 498	−0.007	0.039	Sep 2009–Jun 2016
Mast–h_{ref}	22 225	0.013	0.036	Sep 2009–Jun 2016
Pit–h_{ref}	874	0.053	0.077	Sep 1960–Jun 2017
North pit–h_{ref}	261	0.124	0.128	Sep 2001–Jun 2017
South pit–h_{ref}	261	0.107	0.108	Sep 2001–Jun 2017

sistent measurement period in the Nivose 1 (or mast) sensor was discarded from the comparison. For panel (b), the comparison with the main snow pit field is done over 1960–2017 and for the south and north pits over 2001–2017. For each sensor, the number of points used to calculate the statistics are in Table 5.

Figure 8a and Table 5 show that the three automatic measurements exhibit deviations lower than 1.3 cm and an RMSD lower than 4 cm. Higher discrepancies are found between the automatic reference measurements and the manual measurements (Fig. 8b), with the mean deviation reaching almost 13 cm and RMSD 13 cm. These higher difference values might be attributed to the local slope, aspect, and small topographic features within the three snow pit field areas and to the higher measurement uncertainty associated with manual measurements. Extreme difference values correspond to the end of the snow season when the snow cover is patchy. During the 2014–2015 snow season, Picard et al. (2016) installed an automatic scanning laser 1 metre close to location 6 (Fig. 2) that scanned an area of 100–200 m^2. During this snow season, the laser measurements indicated a spatial variability of the snow depth within the footprint that can reach 7–10 cm (RMSD). Thus, we recommend the use of a $\pm$10 cm uncertainty value for snow depth in any evaluation to represent the spatial variability within the site, comparable to the values used in Lafaysse et al. (2017).

3.3 Water equivalent of snow cover

Figure 9 and Table 6 compare the SWE automatic measurements at location 16 (Fig. 2) with the manual measurements from the main snow pit field (panel a) and the three locations

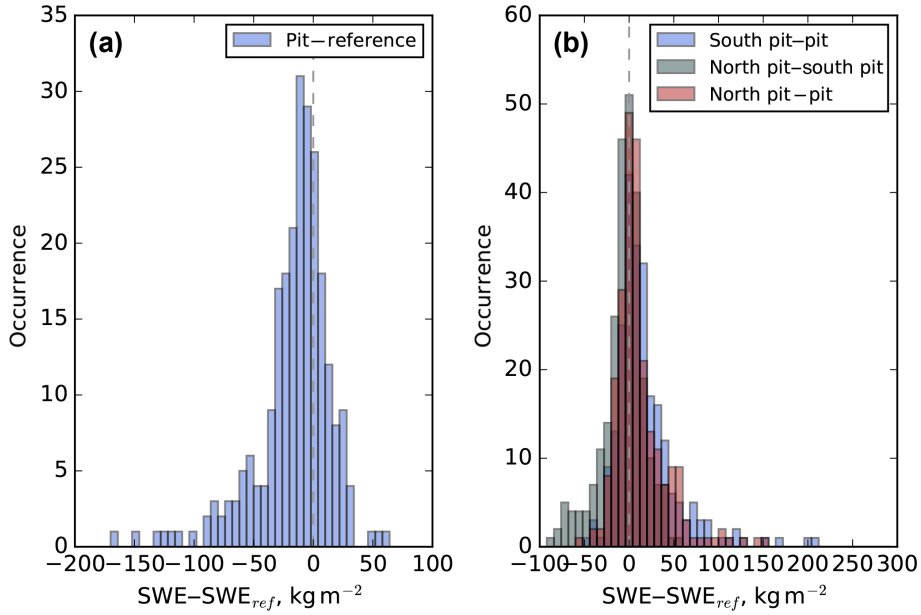

Figure 9. Comparison of SWE measurements at different locations. **(a)** Difference in measured SWE between the manual measurement in the snow pit field (Fig. 2) and the automatic reference SWE (SWE_{ref}, location 16, Fig. 2 in blue). The differences are calculated over the period of 2001–2017 (no reference data for 2015–2016 snow season). Data where both locations indicate 0 SWE are excluded from the statistics. Note that the manual measurements from the south and north snow pit fields are used for the SWE sensor (location 16, Fig. 2) calibration. **(b)** Difference in manually measured SWE between the south snow pit field and the main snow pit field locations in blue, the north and south snow pit field locations in green, and the north snow pit field and the main snow pit field in red. Differences are calculated over the 2001–2017 period. Data where both locations indicate 0 SWE are excluded from the statistics. Numerical values are provided in Table 6.

Table 6. Statistics of the comparisons between the different SWE measurements represented in Fig. 9.

Sensors	Number of dates	Deviation (kg m^{-2})	RMSD (kg m^{-2})	Period
Pit–SWE_{ref}	244	−16.83	24.44	Sep 2001–Jun 2017
South pit–pit	239	17.37	25.09	Sep 2001–Jun 2017
North pit–south pit	260	-6.69	17.66	Sep 2001–Jun 2017
South pit–pit	239	11.84	20.01	Sep 2001–Jun 2017

for manual SWE measurements (panel b). The statistics are calculated over the 2001–2017 period. It must be underlined that the automatic SWE sensor is calibrated using the manual measurements at the south and north snow pit fields. The average of the annual maximum value of SWE_{ref} during this period is 389 ± 104 kg m^{-2}.

Figure 9 and Table 6 show that the mean difference between the automatic and manual measurements in the main snow pit field reaches -17 kg m^{-2} with an RMSD of almost 25 kg m^{-2}. The comparison between the three locations of manual measurements displays an RMSD reaching 25 kg m^{-2}, i.e. 8.6 % of average peak SWE values. This value is consistent with the spatial variability of snow depth and can probably be used as an estimate of the uncertainty associated with the SWE dataset, both due to measurement errors and spatial variability.

3.4 Soil temperature

Figure 10 and Table 7 compare the different soil temperature measurements at 10 and 20 cm depths for locations 23 and 24 (Fig. 2). The left panels in Fig. 10 display the statistics of the different temperature probes at location 23 (Fig. 2), which are spaced by roughly 10 cm (s1_loc23_10, s2_loc23_10, and s3_loc23_10 for 10 cm depths and s1_loc23_20 and s2_loc23_20 for 20 cm depths). It indicates that the RMSD between the three probes is lower than 0.25 K (Table 7). The right panels in Fig. 10 compare locations 24 (Fig. 2) (old sensors) and 23 (new sensors, mean) for two periods: summer (20 June to 10 October) and the snow season (11 October to 19 June). During the snow season, the two locations show a small mean deviation of −0.11 K and an RMSD of 0.42 K, while during summer the mean deviation is roughly −1.06 K,

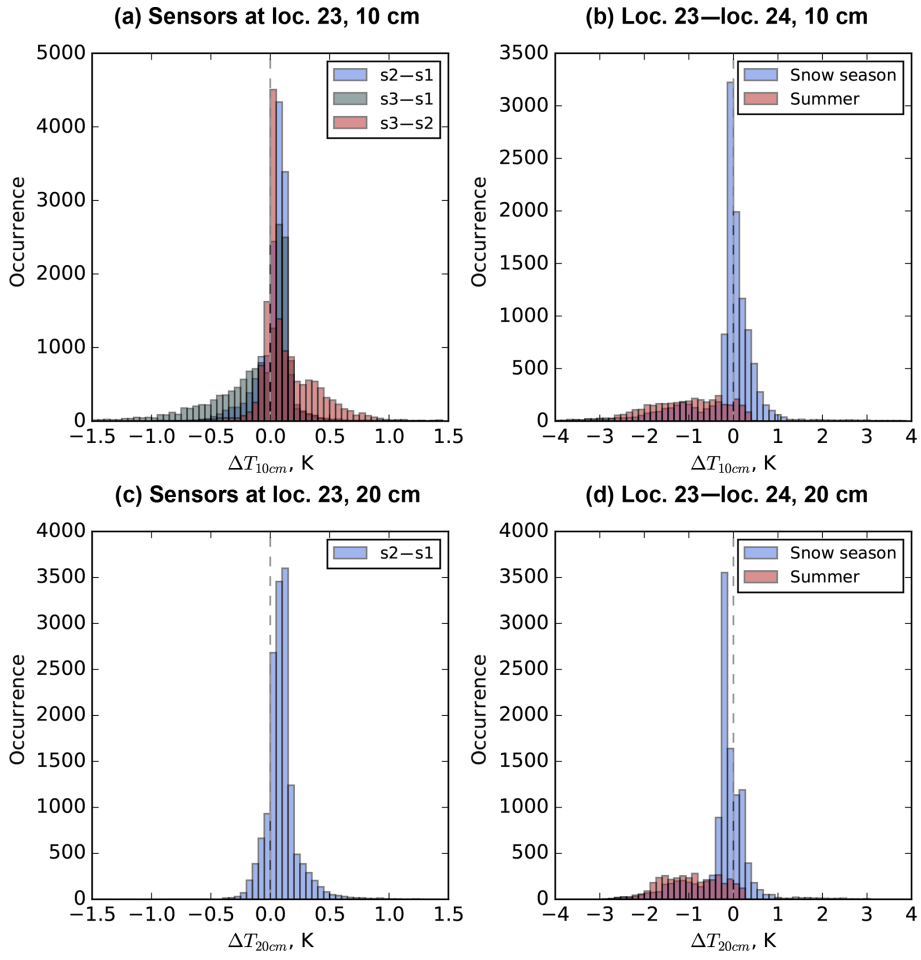

Figure 10. Comparison between the different soil temperature measurements at 10 cm **(a, b)** and 20 cm **(c, d)** depths. Panels **(a)** and **(c)** compare the new sensors (three probes) at location 23 (Fig. 2) at 10 cm underground and two probes at 20 cm underground. Panels **b** and **d** compare the average values of the new sensors (location 23, Fig. 2) to the old ones (location 24, Fig. 2). Statistics are calculated from December 2015 to July 2017. Summer (**b** and **d**, in red) corresponds to the periods between 20 June 2016 and 10 October 2016 as well as 20 June 2017 and 31 July 2017. The rest of the dates correspond to the snow season (**b** and **d**, in blue). Numerical values are provided in Table 7.

Table 7. Statistics of the comparisons between the different soil temperature measurements represented in Fig. 10.

Sensors	Depth (cm)	Number of dates	Deviation (K)	RMSD (K)	Period
s2_loc23_10 – s1_loc23_10	10	15 084	0.034	0.110	Dec 2015–Jun 2017
s3_loc23_10 – s1_loc23_10	10	15 084	−0.094	0.244	Dec 2015–Jun 2017
s3_loc23_10 – s2_loc23_10	10	15 084	0.128	0.182	Dec 2015–Jun 2017
loc_23 – loc_24	10	11 396	−0.108	0.415	Dec 2015–June 2017 (snow season)
loc_23 – loc_24	10	3688	−1.059	1.100	Dec 2015–Jun 2017 (summer)
s2_loc23_20 – s1_loc23_20	20	15 084	0.093	0.118	Dec 2015–Jun 2017
loc_23 – loc_24	20	11 396	−0.224	0.390	Dec 2015–Jun 2017 (snow season)
loc_23 – loc_24	20	3688	−0.943	0.961	Dec 2015–Jun 2017 (summer)

leading to an RMSD of 1.10 K (Table 7). Note that these two locations are spaced by only a few metres (see Fig. 2). The temperature difference between the two sensors may be attributed to differences in soil properties, local topography, and shading. The larger differences in summer may be due to (i) larger heterogeneity in soil wetness and (ii) the absence of the snow cover that spatially tempers the surface temperature signal in winter.

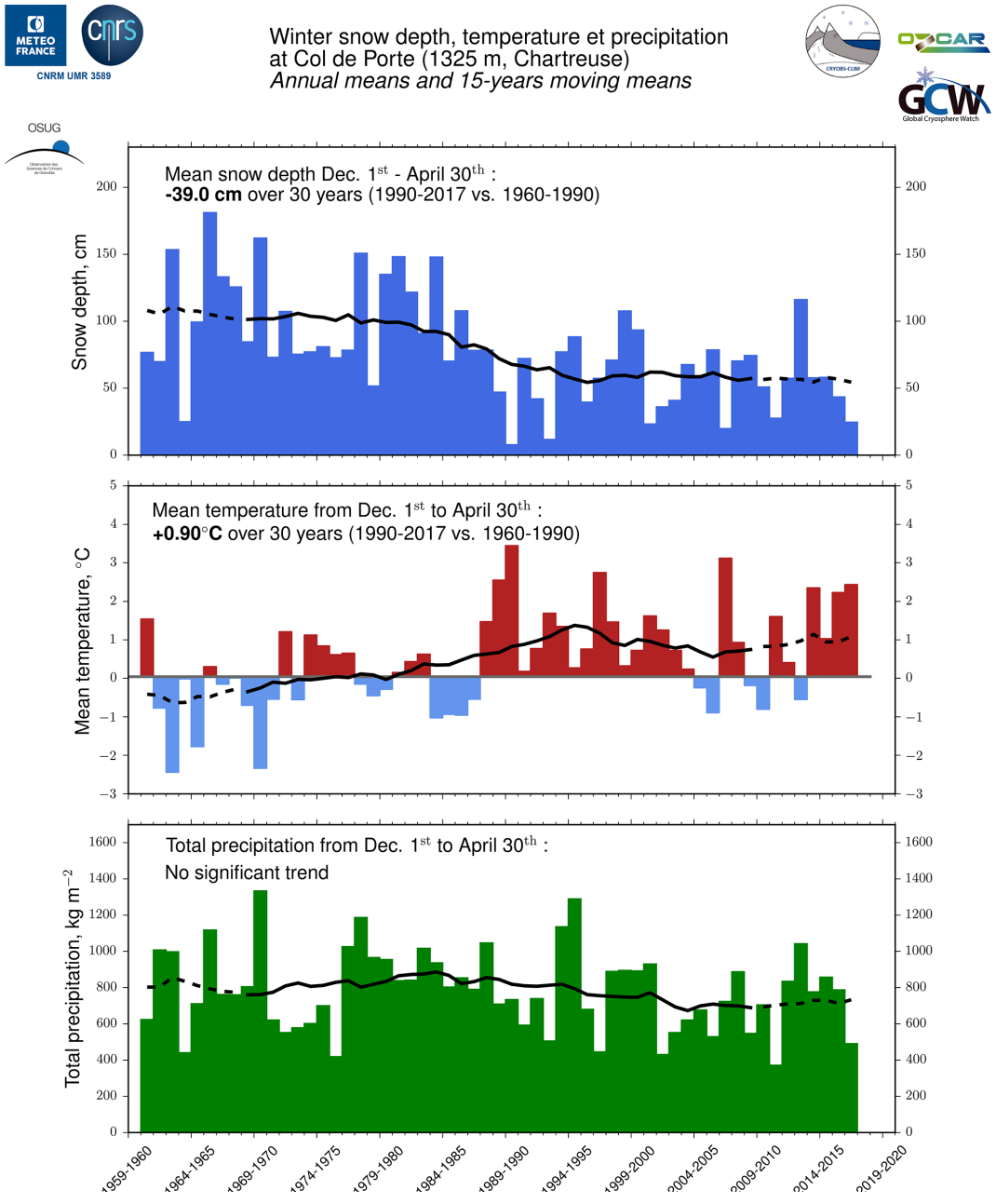

Figure 11. Evolution of mean snow depth, air temperature, and total precipitation over 1960–2017. The mean and total values are calculated over the period of 1 December to 30 April for each snow season. The black lines are 15-year moving means. Figure adapted from Dumont et al. (2018).

From these observations, a lower bound of the uncertainty of the soil temperature measurements (spatial variability and measurements errors) is roughly 1.10 K during summer, roughly 0.42 K during the snow season, and a little higher than 0.5 K averaged over the whole year.

4 Data use

4.1 Temperature, snow depth, and precipitation since 1960

Figure 11 displays the evolution of mean snow depth, air temperature, and total precipitation from 1 December to 30 April of each snow season for the whole period of the dataset (December 1960–April 2017). This figure shows an example of a direct use of the dataset to study the past evolu-

Table 8. Link to the dataset repository.

Dataset	Period	Format	Repository
Solar mask	Jul 1998 and Jun 2018	csv	https://doi.org/10.17178/CRYOBSCLIM.CDP.2018.SolarMask (Lejeune et al., 2018a)
Soil properties	29 Sep 2008 and 2 Oct 2012	csv	https://doi.org/10.17178/CRYOBSCLIM.CDP.2018.Soil (Lejeune et al., 2018b)
Hourly in situ meteorological data	1 Aug 1993 to 31 Jul 2017	netCDF	https://doi.org/10.17178/CRYOBSCLIM.CDP.2018.MetInsitu (Lejeune et al., 2018c)
Hourly SAFRAN meteorological data	1 Aug 1960 to 31 Jul 2017	netCDF	https://doi.org/10.17178/CRYOBSCLIM.CDP.2018.MetSafran (Lejeune et al., 2018d)
Daily snow and meteorological data	1 Aug 1960 to 31 Jul 2017	netCDF	https://doi.org/10.17178/CRYOBSCLIM.CDP.2018.MetSnowDaily (Lejeune et al., 2018e)
Hourly snow data	1 Aug 1960 to 31 Jul 2017	netCDF	https://doi.org/10.17178/CRYOBSCLIM.CDP.2018.HourlySnow (Lejeune et al., 2018f)
Snow profiles	Sep 1993 to Mar 2018	caaml	https://doi.org/10.17178/CRYOBSCLIM.CDP.2018.SnowProfile (Lejeune et al., 2018g)

tion of winter conditions at Col de Porte. It demonstrates that the decrease in mean snow depth between 1960–1990 and 1990–2017 is 39 cm (40 % of the mean snow depth for 1960–1990), while the air temperature has increased by 0.90 °C over the same period, and while the total precipitation does not exhibit a significant trend. This indicates that at this site, the reduction of the snow cover is mainly due to the increase in temperature and its consequences (e.g. higher snow and rain limit during precipitation and higher melt rates). These long time series contribute to placing long-term climate change impact studies on mountain snow conditions in the context of past changes (Verfaillie et al., 2018).

4.2 Snow model evaluation

This dataset has been widely used to drive and evaluate snow models (e.g. Essery et al., 2013; Wever et al., 2014; Magnusson et al., 2015; Decharme et al., 2016; Lafaysse et al., 2017; Piazzi et al., 2018; Krinner et al., 2018). A list of the studies using the CDP dataset is available at http://www.umr-cnrm.fr/spip.php?article533 (last access: 3 Decemebr 2018).

5 Data availability

The database presented and described in this article is available for download at https://doi.org/10.17178/CRYOBSCLIM.CDP.2018 (Cryobs-Clim-CDP, 2018). Table 8 provides the links to the different datasets.

6 Conclusions

This paper describes and provides access to the daily snow and meteorological dataset measured at the Col de Porte site, 1325 m a.s.l., Chartreuse, France, for the period of 1960–2017. The hourly dataset of snow and meteorological observations for the period of 1993–2017 is made available along with weekly snow profiles from September 1993 to March 2018, soil properties, and solar radiation masks. Based on measurements at several locations within the measurement field, we estimated the uncertainties and spatial variability of the ratio between solar diffuse and total irradiance, snow depth, the water equivalent of snow cover, and soil temperature. The data are placed on the repository of the Observatoire des Sciences de l'Univers de Grenoble (OSUG) data centre: http://doi.osug.fr/public/CRYOBSCLIM_CDP/CRYOBSCLIM.CDP.2018.html (last access: 3 December 2018).

Author contributions. YL and JMP endorse the responsibility of the experimental site and of the instruments. MD led the consolidation of the dataset and wrote this manuscript together with all co-authors. EL and JMP ensure the instruments were properly working.

Competing interests. The authors declare that they have no conflict of interest.

Special issue statement. This article is part of the special issue "Hydrometeorological data from mountain and alpine research catchments". It is not associated with a conference.

Acknowledgements. Many thanks are expressed to the people of CNRM and CEN who have assisted in the collection, collation, and archiving of this unique dataset. We thank, in particular, É. Pougatch, Y. Danielou, and J.-L. Dumas for their crucial work on the database. Generating and distributing this dataset directly benefitted from the LABEX OSUG@2020 (ANR10 LABX56). The authors are also thankful to EDF-DTG, ONF, SOERE CryObsClim, GCW, and the IDEX Univ. Grenoble Alpes Cross Disciplinary Project Trajectories. The authors also thank Arnaud Foulquier (LECA) for his help with soil and vegetation property measurements and Laurent Bourges (OSUG) for the establishment of the data repository and the allocation of dedicated DOIs. The

authors are grateful to R. Essery, C. Fierz, and one anonymous referee for their useful comments on the manuscript, and to M. Bavay and C. Fierz for their help with niViz and caaml formats.

Edited by: Danny Marks
Reviewed by: Charles Fierz, Richard L. H. Essery, and one anonymous referee

References

Berliand, M.: Determining the net long-wave radiation of the Earth with consideration of the effect of cloudiness, Izv. Akad. Nauk. SSSR Ser. Geofiz, 1, 64–78, 1952.

Bouilloud, L. and Martin, E.: A coupled model to simulate snow behavior on roads, J. Appl. Meteorol., 45, 500–516, 2006.

Brun, E., David, P., Sudul, M., and Brunot, G.: A numerical model to simulate snow-cover stratigraphy for operational avalanche forecasting, J. Glaciol., 38, 13–22, 1992.

Cryobs-Clim-CDP: Cryobs-Clim-CDP/Col de Porte: a meterological and snow observatory, https://doi.org/10.17178/CRYOBSCLIM.CDP.2018, 2018.

Decharme, B., Martin, E., and Faroux, S.: Reconciling soil thermal and hydrological lower boundary conditions in land surface models, J. Geophys., 118, 7819–7834, https://doi.org/10.1002/jgrd.50631, 2013.

Decharme, B., Brun, E., Boone, A., Delire, C., Le Moigne, P., and Morin, S.: Impacts of snow and organic soils parameterization on northern Eurasian soil temperature profiles simulated by the ISBA land surface model, The Cryosphere, 10, 853–877, https://doi.org/10.5194/tc-10-853-2016, 2016.

Dumont, M., Arnaud, L., Picard, G., Libois, Q., Lejeune, Y., Nabat, P., Voisin, D., and Morin, S.: In situ continuous visible and near-infrared spectroscopy of an alpine snowpack, The Cryosphere, 11, 1091–1110, https://doi.org/10.5194/tc-11-1091-2017, 2017.

Dumont, M., Lejeune, Y., Lafaysse, M., and Morin, S.: Winter at Col de Porte, available at: https://www.ecologique-solidaire.gouv.fr/impacts-du-changement-climatique-montagne-et-glaciers, last access: 10 December 2018.

Durand, Y., Giraud, G., Brun, E., Mérindol, L., and Martin, E.: A computer-based system simulating snowpack structures as a tool for regional avalanche forecasting, J. Glaciol., 45, 469–484, 1999.

Durand, Y., Giraud, G., Laternser, M., Etchevers, P., Mérindol, L., and Lesaffre, B.: Reanalysis of 47 Years of Climate in the French Alps (1958–2005): Climatology and Trends for Snow Cover, J. Appl. Meteor. Climat., 48, 2487–2512, https://doi.org/10.1175/2009JAMC1810.1, 2009a.

Durand, Y., Giraud, G., Laternser, M., Etchevers, P., Mérindol, L., and Lesaffre, B.: Reanalysis of 44 Yr of Climate in the French Alps (1958–2002): Methodology, Model Validation, Climatology, and Trends for Air Temperature and Precipitation., J. Appl. Meteor. Climat., 48, 429–449, https://doi.org/10.1175/2008JAMC1808.1, 2009b.

Essery, R., Morin, S., Lejeune, Y., and Menard, C. B.: A comparison of 1701 snow models using observations from an alpine site, Adv. Water Resour., 55, 131–148, https://doi.org/10.1016/j.advwatres.2012.07.013, 2013.

Essery, R., Kontu, A., Lemmetyinen, J., Dumont, M., and Ménard, C. B.: A 7-year dataset for driving and evaluating snow models at an Arctic site (Sodankylä, Finland), Geosci. Instrum. Method. Data Syst., 5, 219–227, https://doi.org/10.5194/gi-5-219-2016, 2016.

Etchevers, P.: Modélisation de la phase continentale du cycle de l'eau à l'échelle régionale. Impact de la modélisation de la neige sur l'hydrologie du Rhône, PhD thesis, Université Paul Sabatier, Toulouse, 2000.

Etchevers, P., Martin, E., Brown, R., Fierz, C., Lejeune, Y., Bazile, E., Boone, A., Dai, Y.-J., Essery, R., Fernandez, A., Gusev, Y., Jordan, R., Koren, V., Kowalczyk, E., Nasonova, N. O., Pyles, R. D., Schlosser, A., Shmakin, A. B., Smirnova, T. G., Strasser, U., Verseghy, D., Yamazaki, T., and Yang, Z.-L.: Intercomparison of the surface energy budget simulated by several snow models (SNOWMIP project), Ann. Glaciol., 38, 150–158, https://doi.org/10.3189/172756404781814825, 2004.

Fierz, C., Armstrong, R. L., Durand, Y., Etchevers, P., Greene, E., McClung, D. M., Nishimura, K., Satyawali, P. K., and Sokratov, S. A.: The international classification for seasonal snow on the ground, IHP-VII Technical Documents in Hydrology n 83, IACS Contribution n 1, available at: http://unesdoc.unesco.org/images/0018/001864/186462e.pdf (last access: 3 December 2018), 2009.

Gaillardet, J., Braud, I., Hankard, F., et al.: OZCAR, the French network of critical zones observatories, Vadoze Zone J., 17, 180067, https://doi.org/10.2136/vzj2018.04.0067, 2018.

Guyomarc'h, G., Bellot, H., Vionnet, V., Naaim-Bouvet, F., Déliot, Y., Fontaine, F., Puglièse, P., Nishimura, K., Durand, Y., and Naaim, M.: A meteorological and blowing snow dataset (2000–2016) from a high-altitude alpine site (Col du Lac Blanc, France, 2720 m a.s.l.), Earth Syst. Sci. Data, 11, 57–69, https://doi.org/10.5194/essd-11-57-2019, 2019.

Krinner, G., Derksen, C., Essery, R., Flanner, M., Hagemann, S., Clark, M., Hall, A., Rott, H., Brutel-Vuilmet, C., Kim, H., Ménard, C. B., Mudryk, L., Thackeray, C., Wang, L., Arduini, G., Balsamo, G., Bartlett, P., Boike, J., Boone, A., Chéruy, F., Colin, J., Cuntz, M., Dai, Y., Decharme, B., Derry, J., Ducharne, A., Dutra, E., Fang, X., Fierz, C., Ghattas, J., Gusev, Y., Haverd, V., Kontu, A., Lafaysse, M., Law, R., Lawrence, D., Li, W., Marke, T., Marks, D., Nasonova, O., Nitta, T., Niwano, M., Pomeroy, J., Raleigh, M. S., Schaedler, G., Semenov, V., Smirnova, T., Stacke, T., Strasser, U., Svenson, S., Turkov, D., Wang, T., Wever, N., Yuan, H., and Zhou, W.: ESM-SnowMIP: Assessing models and quantifying snow-related climate feedbacks, Geosci. Model Dev. Discuss., https://doi.org/10.5194/gmd-2018-153, in review, 2018.

Lafaysse, M., Cluzet, B., Dumont, M., Lejeune, Y., Vionnet, V., and Morin, S.: A multiphysical ensemble system of numerical snow modelling, The Cryosphere, 11, 1173–1198, https://doi.org/10.5194/tc-11-1173-2017, 2017.

Lejeune, Y., Dumont, M., Panel, J.-M., Lafaysse, M., Lapalus, P., Le Gac, E., Lesaffre, B., and Morin, S.: Solar Masks at Col de Porte site, https://doi.org/10.17178/CRYOBSCLIM.CDP.2018.SolarMask, 2018a.

Lejeune, Y., Dumont, M., Panel, J.-M., Lafaysse, M., Lapalus, P., Le Gac, E., Lesaffre, B., and Morin, S.: Soil properties at Col de Porte site, https://doi.org/10.17178/CRYOBSCLIM.CDP.2018.Soil, 2018b.

Lejeune, Y., Dumont, M., Panel, J.-M., Lafaysse, M., Lapalus, P., Le Gac, E., Lesaffre, B., and Morin, S.: Hourly in situ meteorological data at Col de Porte site, https://doi.org/10.17178/CRYOBSCLIM.CDP.2018.MetInsitu, 2018c.

Lejeune, Y., Dumont, M., Panel, J.-M., Lafaysse, M., Lapalus, P., Le Gac, E., Lesaffre, B., and Morin, S.: Hourly SAFRAN meteorological data at Col de Porte site, https://doi.org/10.17178/CRYOBSCLIM.CDP.2018.MetSafran, 2018d.

Lejeune, Y., Dumont, M., Panel, J.-M., Lafaysse, M., Lapalus, P., Le Gac, E., Lesaffre, B., and Morin, S.: Daily snow and meteorological data at Col de Porte site, https://doi.org/10.17178/CRYOBSCLIM.CDP.2018.MetSnowDaily, 2018e.

Lejeune, Y., Dumont, M., Panel, J.-M., Lafaysse, M., Lapalus, P., Le Gac, E., Lesaffre, B., and Morin, S.: Hourly snow data at Col de Porte site, https://doi.org/10.17178/CRYOBSCLIM.CDP.2018.HourlySnow, 2018f.

Lejeune, Y., Dumont, M., Panel, J.-M., Lafaysse, M., Lapalus, P., Le Gac, E., Lesaffre, B., and Morin, S.: Snow profiles at Col de Porte site, https://doi.org/10.17178/CRYOBSCLIM.CDP.2018.SnowProfile, 2018g.

Magnusson, J., Wever, N., Essery, R., Helbig, N., Winstral, A., and Jonas, T.: Evaluating snow models with varying process representations for hydrological applications, Water Resour. Res., 51, 2707–2723, 2015.

Masson, V., Le Moigne, P., Martin, E., Faroux, S., Alias, A., Alkama, R., Belamari, S., Barbu, A., Boone, A., Bouyssel, F., Brousseau, P., Brun, E., Calvet, J.-C., Carrer, D., Decharme, B., Delire, C., Donier, S., Essaouini, K., Gibelin, A.-L., Giordani, H., Habets, F., Jidane, M., Kerdraon, G., Kourzeneva, E., Lafaysse, M., Lafont, S., Lebeaupin Brossier, C., Lemonsu, A., Mahfouf, J.-F., Marguinaud, P., Mokhtari, M., Morin, S., Pigeon, G., Salgado, R., Seity, Y., Taillefer, F., Tanguy, G., Tulet, P., Vincendon, B., Vionnet, V., and Voldoire, A.: The SURFEXv7.2 land and ocean surface platform for coupled or offline simulation of Earth surface variables and fluxes, Geosci. Model Dev., 6, 929–960, https://doi.org/10.5194/gmd-6-929-2013, 2013.

Morin, S., Lejeune, Y., Lesaffre, B., Panel, J.-M., Poncet, D., David, P., and Sudul, M.: A 18-years long (1993–2011) snow and meteorological dataset from a mid-altitude mountain site (Col de Porte, France, 1325 m alt.) for driving and evaluating snowpack models, Earth Syst. Sci. Data, 4, 13–21, https://doi.org/10.5194/essd-4-13-2012, 2012.

Piazzi, G., Thirel, G., Campo, L., and Gabellani, S.: A particle filter scheme for multivariate data assimilation into a point-scale snowpack model in an Alpine environment, The Cryosphere, 12, 2287–2306, https://doi.org/10.5194/tc-12-2287-2018, 2018.

Picard, G., Arnaud, L., Panel, J.-M., and Morin, S.: Design of a scanning laser meter for monitoring the spatio-temporal evolution of snow depth and its application in the Alps and in Antarctica, The Cryosphere, 10, 1495–1511, https://doi.org/10.5194/tc-10-1495-2016, 2016.

Quéno, L., Karbou, F., Vionnet, V., and Dombrowski-Etchevers, I.: Satellite products of incoming solar and longwave radiations used for snowpack modelling in mountainous terrain, Hydrol. Earth Syst. Sci. Discuss., https://doi.org/10.5194/hess-2017-563, in review, 2017.

Raleigh, M. S., Lundquist, J. D., and Clark, M. P.: Exploring the impact of forcing error characteristics on physically based snow simulations within a global sensitivity analysis framework, Hydrol. Earth Syst. Sci., 19, 3153–3179, https://doi.org/10.5194/hess-19-3153-2015, 2015.

Sauter, T. and Obleitner, F.: Assessing the uncertainty of glacier mass-balance simulations in the European Arctic based on variance decomposition, Geosci. Model Dev., 8, 3911–3928, https://doi.org/10.5194/gmd-8-3911-2015, 2015.

Sicart, J. E., Ramseyer, V., Lejeune, Y., Essery, R., Webster, C., and Rutter, N.: Spatial and Temporal Variabilities of Solar and Longwave Radiation Fluxes below a Coniferous Forest in the French Alps, in: AGU Fall Meeting Abstracts, 2017.

Tuzet, F., Dumont, M., Lafaysse, M., Picard, G., Arnaud, L., Voisin, D., Lejeune, Y., Charrois, L., Nabat, P., and Morin, S.: A multilayer physically based snowpack model simulating direct and indirect radiative impacts of light-absorbing impurities in snow, The Cryosphere, 11, 2633–2653, https://doi.org/10.5194/tc-11-2633-2017, 2017.

Vauge, P. D. B.: Le gisement solaire-Evaluation de la ressource énergétique, Ciel et Terre, 99, 62, 1983.

Verfaillie, D., Lafaysse, M., Déqué, M., Eckert, N., Lejeune, Y., and Morin, S.: Multi-component ensembles of future meteorological and natural snow conditions for 1500 m altitude in the Chartreuse mountain range, Northern French Alps, The Cryosphere, 12, 1249–1271, https://doi.org/10.5194/tc-12-1249-2018, 2018.

Vionnet, V., Brun, E., Morin, S., Boone, A., Martin, E., Faroux, S., Moigne, P. L., and Willemet, J.-M.: The detailed snowpack scheme Crocus and its implementation in SURFEX v7.2, Geosci. Model. Dev., 5, 773–791, https://doi.org/10.5194/gmd-5-773-2012, 2012.

Wever, N., Fierz, C., Mitterer, C., Hirashima, H., and Lehning, M.: Solving Richards Equation for snow improves snowpack meltwater runoff estimations in detailed multi-layer snowpack model, The Cryosphere, 8, 257–274, https://doi.org/10.5194/tc-8-257-2014, 2014.

Williams, C. J., McNamara, J. P., and Chandler, D. G.: Controls on the temporal and spatial variability of soil moisture in a mountainous landscape: the signature of snow and complex terrain, Hydrol. Earth Syst. Sci., 13, 1325–1336, https://doi.org/10.5194/hess-13-1325-2009, 2009.